Dalton Transactions

PAPER

Check for updates

Cite this: *Dalton Trans.*, 2017, **46**, 7273

On the local order of amorphous $La_2Mo_2O_{6.7}$

Jesús Vega-Castillo, *†[a,b,c] Gaëtan Buvat,[c,d] Gwenaël Corbel,[c] Abdelhadi Kassiba,[c] Philippe Lacorre[c] and Alberto Caneiro[a,b,e]

Received 20th February 2017,
Accepted 14th May 2017

DOI: 10.1039/c7dt00637c

rsc.li/dalton

The amorphous reduction product of the oxide ion conductor $La_2Mo_2O_9$ was previously shown to be a good, sulphur-tolerant, anode material for solid oxide fuel cell devices (X. C. Lu, J. H. Zhu, *J. Electrochem. Soc.*, 2008, **155**(10), B1053). In this paper, we study the local order of amorphous $La_2Mo_2O_{6.7}$ using X-ray absorption spectroscopy analyses and electronic paramagnetic resonance. The extended X-ray absorption fine structure analysis of local arrangements around Mo in $La_2Mo_2O_{6.7}$ is first carried out on the basis of strong distortions from three crystalline models of $La_2Mo_2O_9$, $La_7Mo_7O_{30}$ and $La_2Mo_2O_7$. The extended X-ray absorption fits obtained from both $La_2Mo_2O_9$ and $La_7Mo_7O_{30}$ yield similar atomic arrangements in the amorphous phase, upon large atomic displacements. However it is also possible to fit the spectrum using the paths of $La_2Mo_2O_7$, in better agreement with EPR results suggesting the presence of Mo–Mo pairs. Simpler arrangements, built from theoretical single scattering paths, are considered. All models are discussed and compared. A most probable short range structure around Mo in this amorphous phase is proposed. It both fulfills EPR results and appears coherent with the presence of ionic conductivity.

1. Introduction

Since the discovery of oxide-ion conductivity in $La_2Mo_2O_9$,[1] this compound and its derivatives have been subject to intense, either fundamental or applied, research.[2–18] The point is that its ionic conductivity is higher than that of YSZ stabilized zirconia, the reference electrolyte of solid oxide fuel cells, so that it would lower the operating temperature of such devices. A drawback of molybdates is their reducibility in hydrogen, which questions the suitability of $La_2Mo_2O_9$-derived electrolytes in SOFCs without any proper buffer layer. Alternatively, molybdate reduction induces the onset of mixed valence states in molybdenum, which is appropriate to the emergence of electronic conductivity. It is along this line that the most recent developments have come out, with the main focus on an amorphous phase with the composition $La_2Mo_2O_{7-\delta}$. Such a compound has been successfully tested as a sulfur-tolerant mixed ionic-electronic anode in SOFC devices[19] stable on the mid-term.[20] Lately, a partly oxidized form of this reduced amorphous phase at the surface of nanowires has been proposed to be at the origin of a huge increase in ionic conductivity measured on such nanowires.[21] The growing interest in such a reduced amorphous phase $La_2Mo_2O_{7-\delta}$ prompted us to probe the salient features of its local structural arrangement. For this purpose, X-Ray Diffraction (XRD), Electronic Paramagnetic Resonance (EPR) and X-ray Absorption Spectroscopy (XAS) were used on amorphous samples with the composition $La_2Mo_2O_{6.7}$. Extended X-ray Absorption Fine Structure (EXAFS) measurements were also made on crystallized samples with compositions $La_2Mo_2O_9$ and $La_7Mo_7O_{30}$, and also calculation on a $La_2Mo_2O_7$ model, for comparison purposes.

After the Experimental section (section 2), the presentation of Results and discussion (section 3) will be structured as follows. In a first step, we will focus on the local order of crystallized phases in the $La_2Mo_2O_{9-y}$ system as evidenced by XRD (section 3.1). Then analyses of the EXAFS spectra of these forms will be used as bases to the possible local order of the amorphous reduced form (section 3.2). At this point, analysis of the EPR spectrum of $La_2Mo_2O_{6.7}$ will help us to bring out a salient feature of its local order (section 3.3). Ultimately, a step by step building of an amorphous model will be carried out, using both the EXAFS profile and previous element (section 3.4). Finally, summary and a conclusion will be given in section 4.

[a]*Centro Atómico Bariloche - Instituto Balseiro, Av. Bustillo 9500, 8400 San Carlos de Bariloche, Argentina. E-mail: jvegacastillo@ifisur-conicet.gob.ar*
[b]*Consejo Nacional de Investigaciones Científicas y Técnicas CONICET, Argentina*
[c]*Institut des Molécules et Matériaux du Mans (IMMM), Univ. Bretagne-Loire, UMR CNRS 6283, Univ. Maine, avenue Olivier Messiaen, F-72085 Le Mans Cedex 9, France*
[d]*Institut des Matériaux Jean Rouxel (IMN), Univ. Bretagne-Loire, UMR CNRS 6502, Univ. Nantes, 2 rue de la Houssinière, BP32229 F-44322 Nantes Cedex 3, France*
[e]*Comisión Nacional de Energía Atómica CNEA, Argentina*
† Present address: Instituto de Física del Sur IFISUR, Av. Alem 1253, 8000 Bahía Blanca, Buenos Aires, Argentina.

2. Experimental

$La_2Mo_2O_9$ powder samples were prepared by a standard solid state reaction, starting from La_2O_3 and MoO_3. La_2O_3 was previously annealed at 1000 °C for 1 h for dehydration and decarbonation. Stoichiometric amounts of precursors were ground manually in an agate mortar. The mixture was annealed first at 500 °C for 12 h and then at 900 °C for 12 h. After this heat treatment, the powders were ground and annealed at the same temperature again. This process was repeated until pure $La_2Mo_2O_9$ was obtained.

The purity of the samples was verified by X-ray Diffraction (XRD) using a Philips PW1700 and a PANalytical θ/θ Bragg–Brentano X'pert MPD PRO diffractometer (CuKα1 + 2 radiation) equipped with the X'Celerator multi-element detector.

The amorphous sample studied by EXAFS was prepared in a modified Cahn 1000 electrobalance.[22] Approximately 500 mg of $La_2Mo_2O_9$ powders were reduced at 608 °C until amorphization, in flowing Ar–(10%)H_2 at a flow rate of 6 L h^{-1}, resulting in the composition $La_2Mo_2O_{6.72}$. $La_7Mo_7O_{30}$ was prepared by partial reduction of $La_2Mo_2O_9$ powders in the Thermogravimetric Analysis (TGA) apparatus at 718 °C in an Ar–H_2–H_2O mixture as described elsewhere.[23,24] The amorphous sample studied by EPR was also prepared in a TGA balance at 700 °C for 9 h in Ar–(10%)H_2 flowing at 4.8 L h^{-1}, leading to the composition $La_2Mo_2O_{6.7}$.

Electron spin resonance measurements were performed on an EPR Bruker EMX19 apparatus equipped with a 9.5 GHz X band. The used instrumental parameters are set to 100 kHz for the modulation frequency and 10 Gauss for the field modulation, *i.e.* well below the individual line width in order to prevent any line shape distortion. A powder sample (50 mg) of $La_2Mo_2O_{6.7}$ was placed in a Suprasil quartz tube and the fitted resonant cavity was mounted with an Oxford Instrument cryostat dedicated to record the EPR spectra with better resolved details at low temperatures. Analysis of the EPR spectra was made by using Bruker software Winsimfonia which allows evaluating the EPR spectral parameters required to identify the nature of involved paramagnetic centers, the symmetry of their local environments as well as the strength of their mutual interactions.

X-ray Absorption Spectroscopy (XAS) experiments, scanning Near Edge (XANES) and EXAFS zones, at the K-edge of Mo were performed at the Labóratorio Nacional de Luz Síncrotron (LNLS), Campinas, Brazil. The spectra were collected in transmission mode at the lines D04B and XDS; the latter counts with a superconducting multipole wiggler which allows generating a significantly higher flux of photons. Metallic Mo was used as a reference for aligning the spectra. The reduction of data and analysis of EXAFS zones were made with the programs ATHENA and ARTHEMIS.[25] The passive electron reduction factors S_0^2 were obtained from adjusting the EXAFS spectra of metallic Mo. This factor was fixed during the analyses of the lanthanum molybdate samples. The mean square displacements σ^2 were set as equal for shells of the same atom separated for no longer than 0.2 Å. One common energy shift ΔE_0 was used for all the shells included in each fit.

3. Results and discussion

3.1 Structural analysis of $La_2Mo_2O_{9-y}$ crystallized and amorphous forms

Fig. 1 shows the evolution as a function of time of oxygen content in a $La_2Mo_2O_9$ powder under a 6 L h^{-1} flow of Ar–H_2(10%) at 608 °C, leading ultimately to amorphous $La_2Mo_2O_{6.72}$. In the figure, the dashed horizontal lines indicate the oxygen content of 3 definite crystalline compounds of the system which are not stable under these conditions, namely $La_2Mo_2O_9$, $La_7Mo_7O_{30}$ and $La_2Mo_2O_7$.

The structures of the three crystallized phases, shown in Fig. 2, can be quickly described as follows:

- The $La_2Mo_2O_9$ structure consists of more or less disordered oxide ions surrounding a slightly distorted parallelepipedic lattice whose corners are occupied alternately by La and Mo cations with various distorted O^{2-} environments (coordination tetrahedra of Mo^{6+} are isolated),[6]

- $La_7Mo_7O_{30}$ is built up from corner-sharing MoO_6 octahedra forming columns of perovskite cages (interconnected by their diagonal opposite sides) inserting and surrounded by La^{3+} ions,[26]

- The $La_2Mo_2O_7$ structure is made of corner and edge-sharing MoO_6 octahedra forming stepped sheets of ribbons surrounded by La^{3+} cations.[27]

The right part of Fig. 2 displays, for each of these compounds, the local environment of Mo cations in terms of O^{2-} coordination shells and of La/Mo closest neighbours. It is to be noted that the most reduced these compounds are, the closest to each other the Mo ions are located, in their respective structures (shortest Mo–Mo distances are ~4.63 Å in $La_2Mo_2O_9$, 4.008 Å in $La_7Mo_7O_{30}$, and 2.478 Å in $La_2Mo_2O_7$).

After reduction for about 50 hours, the sample which reached the oxygen content $O_{6.72}$ was quenched, and its XRD pattern showed that it was amorphous. In Fig. 3, we have superimposed the XRD pattern of $La_2Mo_2O_9$ (top) and amorphous

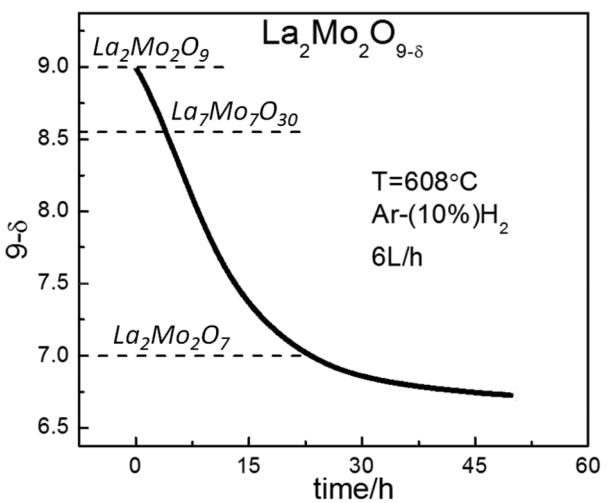

Fig. 1 Thermogravimetric curve of the reduction of a $La_2Mo_2O_9$ powder at 608 °C in diluted H_2.

This journal is © The Royal Society of Chemistry 2017

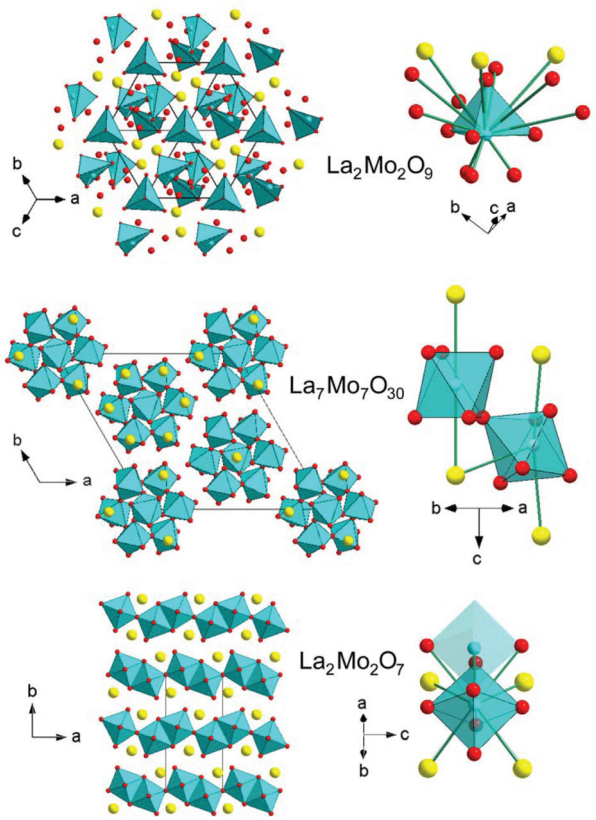

Fig. 2 Global configuration (left) and local arrangement around Mo (right) in the structures of crystallized β-$La_2Mo_2O_9$ (upper), $La_7Mo_7O_{30}$ (middle) and $La_2Mo_2O_7$ (lower). Mo coordination polyhedra are in blue as well as Mo ions, La^{3+} ions are in yellow and O^{2-} ions in red. Note that Mo coordination polyhedra are isolated in $La_2Mo_2O_9$, corner-sharing in $La_7Mo_7O_{30}$, and edge-sharing in $La_2Mo_2O_7$.

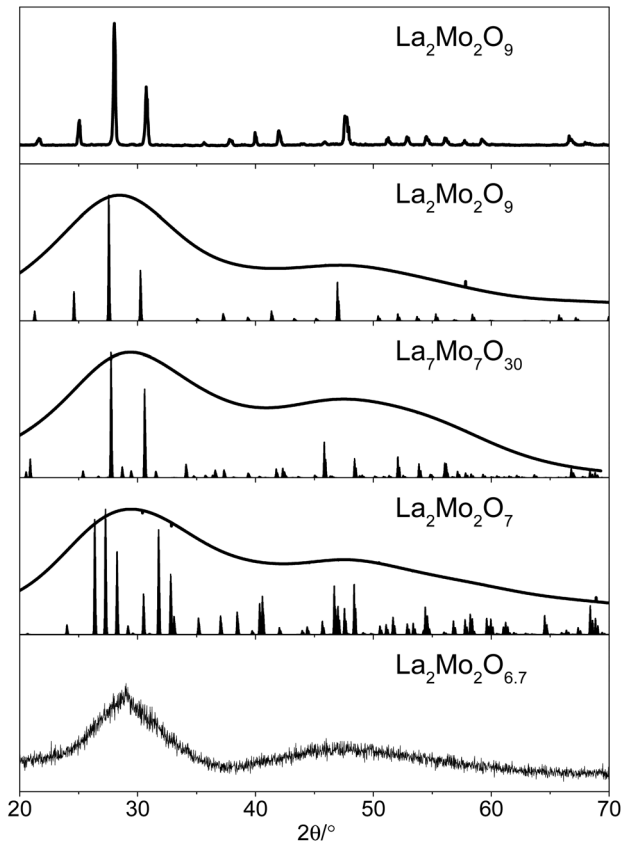

Fig. 3 XRD pattern of $La_2Mo_2O_9$ (top) and amorphous $La_2Mo_2O_{6.72}$ (bottom) with in between simulated XRD patterns of $La_2Mo_2O_9$, $La_7Mo_7O_{30}$ and $La_2Mo_2O_7$ assuming large (narrow peaks) and very small crystallite sizes (broad envelopes) from PDF4+ database software.[28]

$La_2Mo_2O_{6.72}$ (bottom) with a simulation of the XRD patterns of crystalline $La_2Mo_2O_9$, $La_7Mo_7O_{30}$ and $La_2Mo_2O_7$ (from the PDF-4+ database[28]). The envelope above the simulated crystalline patterns is obtained by drastically reducing, through the simulation software, the crystallite size to a few angstroms. This last trick is assumed to mimic a phase amorphization by reducing the coherence length to a few neighbouring shells, and then to reproduce an amorphous phase that would have maintained the local ordering of the original crystalline phase.

One can clearly see in Fig. 3 that the "amorphous" patterns issued from the crystalline phases are very close to each other, and to that of amorphous $La_2Mo_2O_{6.72}$, with two broad bumps. It seems impossible to deduce, from such XRD pattern simulations, if the local structural arrangement in amorphous $La_2Mo_2O_{6.72}$ is closest to that of $La_2Mo_2O_9$, of $La_7Mo_7O_{30}$ or of $La_2Mo_2O_7$. We therefore decided to use spectroscopic techniques, such as XAS and EPR, to gain more information about it.

3.2 XAS analysis of crystallized forms as the base for the amorphous model

In our previous studies on the thermodynamic stability of $La_2Mo_2O_9$ under low oxygen pressure at 608 °C and 718 °C, several reduced phases had been evidenced, including $La_7Mo_7O_{30}$ and the amorphous reduced phase.[23] At higher temperature (1000 °C) other reduced crystalline phases with different La : Mo balances were isolated.[29] At these three temperatures, crystalline $La_2Mo_2O_7$ has never been observed (which does not mean that it could not be stable at any other – intermediate – temperature). Until now crystalline $La_2Mo_2O_7$ has only been prepared under very specific conditions by fused salt electrolysis[27] or by ball milling.[30] For the current study as in the previous, the reduced $La_7Mo_7O_{30}$ and amorphous samples were obtained by the reduction of $La_2Mo_2O_9$ prepared by the solid state reaction (see the Experimental section). Crystalline $La_2Mo_2O_7$ was not studied experimentally, but its structure was used, as well as those of $La_2Mo_2O_9$ and $La_7Mo_7O_{30}$, as one of the initial configurations for the refinement of the local environment of amorphous $La_2Mo_2O_{6.72}$ from EXAFS analysis using FEFF paths.

To begin with, the XANES zones of XAS spectra in the K-edge of Mo for $La_2Mo_2O_{9-\delta}$ compounds and metallic Mo are shown in Fig. 4(a). As observed, the absorption edge shifts to a higher energy as the oxidation state of Mo increases. Fig. 4(b), (c) and (d) show the fitting of the edges of $La_2Mo_2O_9$, $La_7Mo_7O_{30}$ and $La_2Mo_2O_{6.72}$ respectively. The jump corres-

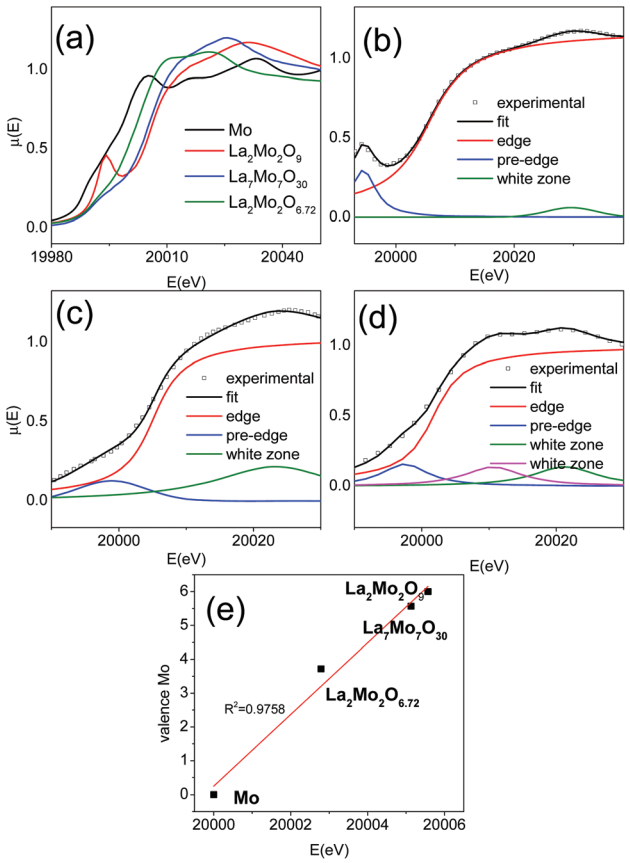

Fig. 4 (a) Comparison of normalized molybdenum K-edge XANES data collected at room temperature on different molybdates and metallic Mo; fit of the edge, pre-edge and white zone for XANES analysis of: (b) $La_2Mo_2O_9$, (c) $La_7Mo_7O_{30}$ and (d) amorphous $La_2Mo_2O_{6.72}$; (e) valence of Mo as a function of the energy of the edge E_0.

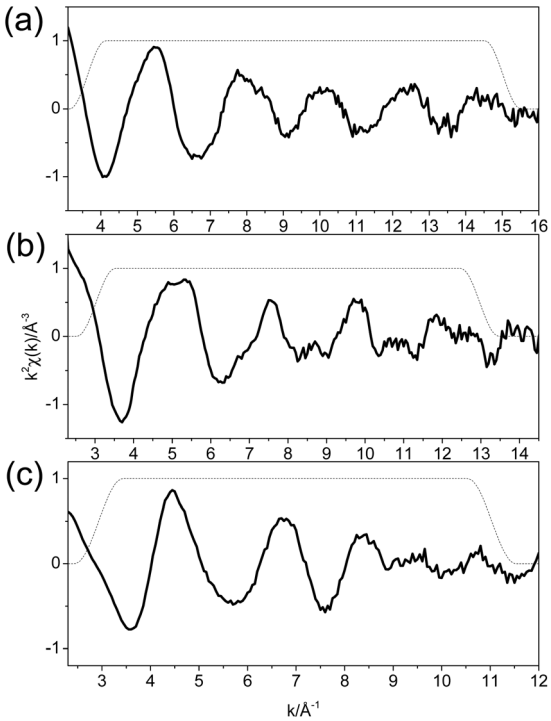

Fig. 5 EXAFS signal multiplied by k^2 and the selected range for FT for: (a) crystalline $La_2Mo_2O_9$, (b) crystalline $La_7Mo_7O_{30}$ and (c) amorphous $La_2Mo_2O_{6.72}$.

ponding to the edge itself was fitted with an arctangent function whereas the crest after the edge, known as the white line, was fitted with the Gaussian function(s). The centroid of each arctangent corresponds to the edge energy E_0.

The valence of Mo deduced from TGA measurements in the different analysed compounds as a function of E_0 is shown in Fig. 4(e). A linear dependence is noticeable with the formula:

$$\text{Valence Mo} = 1.05967E_0 - 21\,193.9484. \quad (1)$$

With this formula the valence of Mo in the amorphous yields 3.26 compared to 3.72 calculated based on the oxygen content. This discrepancy might arise from the small non-linearity of the dependence of the valence on the edge energy.

After extraction from the absorption spectrum, Fourier Transform (FT) was applied to the EXAFS signal multiplied by the square of the wave number k within the ranges shown in Fig. 5.

In order to analyse the local structure of the amorphous phase we started from models corresponding to those of the crystalline phases of the system – namely $La_2Mo_2O_9$, $La_7Mo_7O_{30}$ and $La_2Mo_2O_7$ (see the right part of Fig. 2) – and allowed large atomic displacements as well as the corresponding oxygen loss, to fit with the $La_2Mo_2O_{6.72}$ data.

The amplitudes and scattering functions for the analyses of the EXAFS signals of $La_2Mo_2O_9$ and $La_7Mo_7O_{30}$ and the amorphous compound starting from three crystalline arrangements were calculated with FEFF[31] into ARTEMIS software, using single scattering paths only. A length degeneracy fuzziness of 0.03 Å (the default value in ARTEMIS) was set, so two paths with lengths differing by less were considered degenerate.

3.2.1 Crystallized $La_2Mo_2O_9$ and amorphous $La_2Mo_2O_{6.72}$ (model 1). The crystal structure of the low temperature form α-$La_2Mo_2O_9$[32] contains 96 independent cationic and 216 independent oxygen sites, while that of the high temperature form β-$La_2Mo_2O_9$ has only 2 independent cationic sites and 3 independent oxide sites, whose O2 and O3 positions are partially occupied with large anisotropic thermal factors.[6] Malavasi *et al.*[33] have shown, thanks to neutron atomic pair distribution function (PDF) analysis, that the local structure of the cubic β-$La_2Mo_2O_9$ phase is exactly the same as that of the monoclinic α phase, thus indicating that the structural phase transition is actually a transition from a static to a dynamic distribution of the oxygen defects. Because of the complexity of the structure of α-$La_2Mo_2O_9$ and the similarity of the local structure in both polymorphs, the calculation of amplitudes and scattering functions around Mo for α-$La_2Mo_2O_9$ from EXAFS data was then made on the basis of the cubic crystal structure of the high temperature β phase reported by Georges *et al.*[6] The fitting was made up to a distance of 3.6 Å from Mo, including 6 coordination spheres as listed in Table 1.

This journal is © The Royal Society of Chemistry 2017

Table 1 Single scattering paths calculated by FEFF for β-$La_2Mo_2O_9$ (N and R_0) and results from fitting the EXAFS spectrum of crystallized $La_2Mo_2O_9$ and amorphous $La_2Mo_2O_{6.72}$ (ΔE_0, R, σ^2 and Occ) with 6 coordination shells[a]

				R/Å		σ^2/Å^2		Occ		Ncoor	
Shell	Atom	N	R_0/Å	$La_2Mo_2O_9$	Amorphous	$La_2Mo_2O_9$	Amorphous	$La_2Mo_2O_9$	Amorphous	$La_2Mo_2O_9$	Amorphous
1	O3	3	1.6873	*1.801*	*2.082*	*0.00189*	*0.00198*	*0.43*	*0.345*	1.29	1.035
2	O2	3	1.7375	*1.799*	*1.976*	*0.00189*	*0.00198*	*0.73*	*0.444*	2.19	1.332
3	O1	1	1.8190	*1.987*	*2.057*	*0.00189*	*0.00198*	1	1	1	1
4	O3	3	3.3868	*3.397*	*2.536*	*0.00748*	*0.00285*	*0.43*	*0.345*	1.29	1.035
5	O3	3	3.4683	*3.449*	*2.537*	*0.00748*	*0.00285*	*0.43*	*0.345*	2.19	1.035
6	La1	3	3.6610	*3.591*	*2.584*	*0.01458*	*0.01387*	1	1	3	3

[a] S_0^2 = 0.928 ($La_2Mo_2O_9$ and amorphous); ΔE_0(eV) = 3.926 ($La_2Mo_2O_9$), 3.598 (amorphous); R-factor = 0.0158 ($La_2Mo_2O_9$), 0.0081 (amorphous).

In the crystalline structure of β-$La_2Mo_2O_9$ the O2 and O3 sites are partially occupied with site occupancy factors of 0.78 and 0.378, respectively.[6] O2 and O3 occupy the positions 12b while O1 are in positions 4a of the space group $P2_13$, with 2 formula units per cell. Therefore, the total oxygen content y in $La_2Mo_2O_y$ can be calculated as:

$$y = 6(\mathrm{occO2} + \mathrm{occO3} + 2). \quad (2)$$

The occupancy is not taken into account for FEFF calculation, but it was included into the posterior EXAFS fitting based on the calculated paths. The passive electron reduction factor was multiplied by the occupancy of the given shell. OccO2 and OccO3 where restrained to fulfil eqn (2) with y = 9.

The EXAFS spectra in the real space R and its fit with 6 shells, until the first shell of La, are shown in the left part of Fig. 6 in magnitude (upper) and its real part (lower).

The values obtained from the analysis of the EXAFS spectrum of $La_2Mo_2O_9$ are given in Table 1. The values of distances R, with respect to Mo for each sphere, are slightly different from the initial R_0 ones calculated by FEFF for β-$La_2Mo_2O_9$. This difference might be due to the approximation made of the measured α phase to the β one.

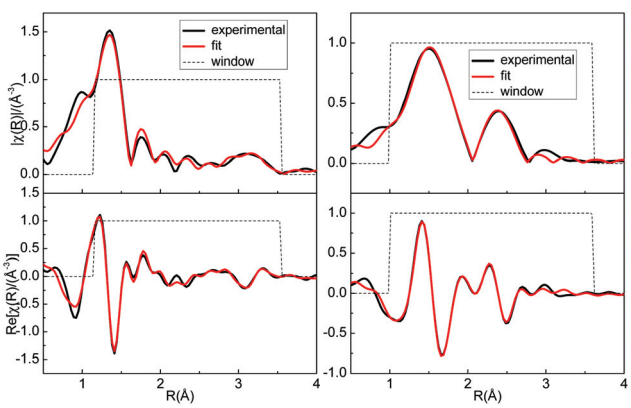

Fig. 6 Fourier transform of EXAFS oscillations at the molybdenum K-edge for $La_2Mo_2O_9$ (left) and $La_2Mo_2O_{6.72}$ (right): modulus (upper) and real part (lower). Red lines show the fit of EXAFS data with 6 coordination shells around Mo.

The fit of the FT of the EXAFS spectrum measured for amorphous $La_2Mo_2O_{6.72}$, using the 6 paths described in Table 1 for $La_2Mo_2O_9$, is shown in Fig. 6, right part. The occupancies of O2 and O3 were restrained to fulfil eqn (2) with y = 6.72.

The results obtained from the fitting of EXAFS of the amorphous compound are also shown in Table 1. They would appear to be consistent with a partial preservation of a short range order of LAMOX structure in the amorphous material, with large displacements of the shells neighbouring Mo. According to the results, upon amorphization the three first oxygen shells (O3, O2 and O1) would move away from Mo, whereas the next two shells of oxygens (both O3) and the one of La would move towards Mo.

The arrangement model obtained this way can be understood as three main shells: the first one of O (including shells 1, 2 and 3) at an R around 2 Å and a second one of La at ~2.6 Å. There is also an intermediate shell of O (shells 4 and 5) at 2.5 Å. One can calculate the coordination number of each shell by adding the product of N times Occ for each main shell as shown in Table 2.

Fig. 7 shows a scheme of the coordination shells (projected in two dimensions) around Mo, obtained from EXAFS analysis for (a) $La_2Mo_2O_9$ and (b) amorphous $La_2Mo_2O_{6.72}$ within a $La_2Mo_2O_9$ type model of the local order. In the illustration, O2 and O3 shells are fully occupied. The distribution of atoms in each shell is arbitrary since the EXAFS structure does not give information on this variable.

In β-$La_2Mo_2O_9$ the average coordination number of Mo, taking into account the closeness of the three first O shells, and the partial occupancies of O2 and O3, is ~4.5.[34] If one makes this calculation with the same three first shells and the occupancy factors obtained from EXAFS analysis for the amorphous compound, the coordination number would yield 3.27.

Table 2 Coordination numbers and average distances of the arrangement model based on $La_2Mo_2O_9$ paths around Mo, summarized as three main shells

# Main shell	Atom	Ncoor	Average R
1st	O	3.367	2.03
Intermediate	O	2.07	2.54
2nd	La	3	2.58

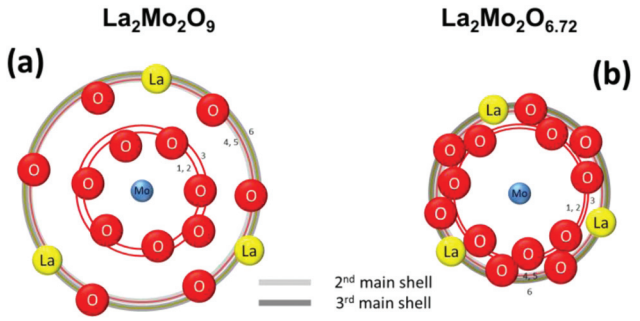

Fig. 7 Schemes of coordination shells around Mo, obtained from EXAFS analysis in: (a) crystalline $La_2Mo_2O_9$; (b) amorphous $La_2Mo_2O_{6.72}$ within a $La_2Mo_2O_9$ type model of the local order.

In the literature the minimum coordination reported for Mo is 4 in the oxidation state +6 and 6 in states +3 and +4.[35] The presumable instability of Mo^{3+}/Mo^{4+} in coordination 3.27 could be the cause of the atomic merging of the next coordination shells, in order to increase the average coordination number.

The distancing of the three first O3, O2 and O1 coordination spheres could be explained by the increase of the ionic radius of Mo upon going from +6 valence to a mixed +4/+3. Finally, La and Mo get closer by 1.007 Å and this would be due to the decrease of electrostatic repulsion between the two cations, because of the partial reduction of the latter.

3.2.2 Crystallized $La_7Mo_7O_{30}$ and amorphous $La_2Mo_2O_{6.72}$ (model 2). The crystalline structure of $La_7Mo_7O_{30}$ has been resolved by Goutenoire *et al.*[26] in the space group $R\bar{3}$. It has two Mo sites, Mo1 and Mo2, fully occupying positions 3b and 18f, respectively; in other words there is one Mo1 for every six Mo2. This structure was used for generating a list of single scattering paths around both Mo1 and Mo2 using FEFF in Artemis software. Two paths around Mo1 and six paths around Mo2 were utilized for fitting the experimental EXAFS spectrum of $La_7Mo_7O_{30}$; the list of used paths is shown in Table 3. The passive electron reduction factor S_0^2, previously obtained from the EXAFS fit of Mo reference foil, was multiplied by 1/7 and 6/7 for Mo1 and Mo2 paths respectively for taking into account the multiplicity of the respective sites.

The fitting of $La_7Mo_7O_{30}$ is shown in Fig. 8 left part, for magnitude (upper) and real part (lower). The results are listed in Table 3. These paths were used afterwards for attempting to fit the EXAFS spectrum of amorphous $La_2Mo_2O_{6.72}$.

The formation of the perovskite related compound $La_7Mo_7O_{30}$ ($La_2Mo_2O_{8.57}$) from partially reducing $La_2Mo_2O_9$ has been reported by some authors at 760 °C (ref. 26) and at 718 °C.[23,24] In these studies this crystalline reduced molybdate appears as an intermediate state prior amorphization. Although at 608 °C, as shown in Fig. 1, the reduction is continuous from $La_2Mo_2O_9$ to amorphous, it could happen that the amorphous sample $La_2Mo_2O_{6.72}$ adopts a short range arrangement closer to that of $La_7Mo_7O_{30}$ than to that of $La_2Mo_2O_9$. It is this hypothesis that we will now test.

Once again the passive electron reduction factor was multiplied by 1/7 and 6/7 for paths around Mo1 and Mo2 respectively. Also, a partial occupancy of 0.784 was set for each O shell in order to set the total oxygen content to 6.72.

The result of fitting the EXAFS spectra of amorphous $La_2Mo_2O_{6.72}$ using the same paths as for $La_7Mo_7O_{30}$ fitting is

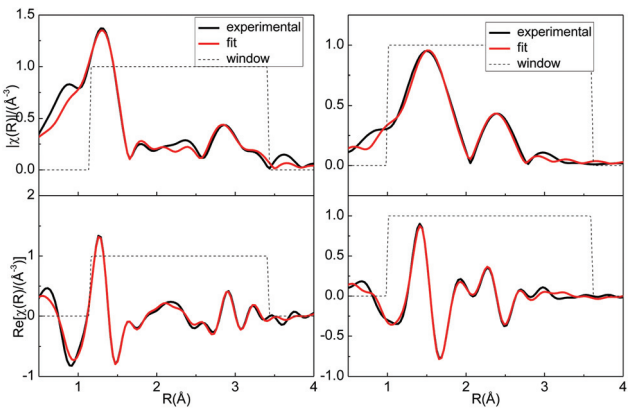

Fig. 8 Fourier transform of EXAFS oscillations at the molybdenum K-edge for $La_7Mo_7O_{30}$ (left) and $La_2Mo_2O_{6.72}$ (right): modulus (upper) and real part (lower). Red lines show the fit of EXAFS data with 8 coordination shells around two Mo sites.

Table 3 Single scattering paths calculated for $La_7Mo_7O_{30}$ (N and R_0) and results from fitting the EXAFS spectrum of crystallized $La_7Mo_7O_{30}$ and amorphous $La_2Mo_2O_{6.72}$ (ΔE_0, R and σ^2) with 8 coordination shells around two Mo sites[a]

						R/Å		σ^2/Å^2	
Shell	Central atom	Atom	N	Weight	R_0/Å	$La_7Mo_7O_{30}$	Amorphous	$La_7Mo_7O_{30}$	Amorphous
1	Mo1	O5	6	1/7	1.9917	*1.942*	*2.149*	*0.00194*	*0.00278*
2	Mo1	La1	2	1/7	3.4303	*3.718*	*2.993*	*0.00558*	*0.00721*
3	Mo2	O4	1	6/7	1.7742	*1.831*	*2.063*	*0.00194*	*0.00278*
4	Mo2	O2	2	6/7	1.8216	*1.832*	*2.023*	*0.00194*	*0.00278*
5	Mo2	O3	1	6/7	1.9358	*1.998*	*2.018*	*0.00194*	*0.00278*
6	Mo2	O5	2	6/7	2.2044	*2.164*	*2.533*	*0.00912*	*0.00133*
7	Mo2	La2	2	6/7	3.4609	*3.163*	*2.616*	*0.00821*	*0.01302*
8	Mo2	La1	1	6/7	3.4846	*3.517*	*2.530*	*0.00558*	*0.01302*

[a] S_0^2 = 1.214 ($La_7Mo_7O_{30}$), 0.928 (amorphous); ΔE_0(eV) = −3.932 ($La_7Mo_7O_{30}$), 2.315 (amorphous); R-factor = 0.0073 ($La_7Mo_7O_{30}$), 0.0129 (amorphous).

This journal is © The Royal Society of Chemistry 2017

shown in Fig. 8, right part, for magnitude (upper) and real part (lower). As observed, the fit has a similar quality to that based on $La_2Mo_2O_9$ paths previously obtained (see Fig. 6, right part).

The summary of the results of the EXAFS fit of the amorphous with model 2 is listed in Table 3. The arrangement in model 2 can also be understood as three main shells: a first shell of O (including paths 1, 3, 4 and 5), a second one of La (paths 2, 7 and 8) and an intermediate one of O (shell 6). The coordination numbers, calculated by adding the product of *N* times Occ times weight, and average distances *R*, are listed in Table 4. The resulting coordination numbers calculated for the first and second shells are very close to those obtained from model 1 whereas the intermediate O shell is almost half (see Table 2). The similar results in Tables 2 and 4 for the first and second main shells led us to conclude that the obtained arrangements for the amorphous phase starting from $La_2Mo_2O_9$ and $La_7Mo_7O_{30}$ models are somehow equivalent in spite of the significant differences between the original crystalline structures. The scheme of this atomic arrangement would be that shown in Fig. 7(b).

3.2.3 Crystallized $La_2Mo_2O_7$ and amorphous $La_2Mo_2O_{6.72}$ (model 3). The oxygen stoichiometry of $La_2Mo_2O_7$ is very close to that of $La_2Mo_2O_{6.72}$. No experimental EXAFS spectrum of $La_2Mo_2O_7$ was available, so the single scattering paths around the lone Mo site of $La_2Mo_2O_7$ were generated by FEFF and directly used for fitting the EXAFS spectrum of the amorphous compound. The 7 used paths are listed in Table 5. The degeneracy *N* of each O shell was multiplied by 0.96 to set the total oxygen content to 6.72.

The magnitude (a) and real part (b) of the experimental EXAFS spectrum of amorphous $La_2Mo_2O_{6.72}$ along with the resulting fitting are shown in Fig. 9, as observed, the fit yields an acceptable match.

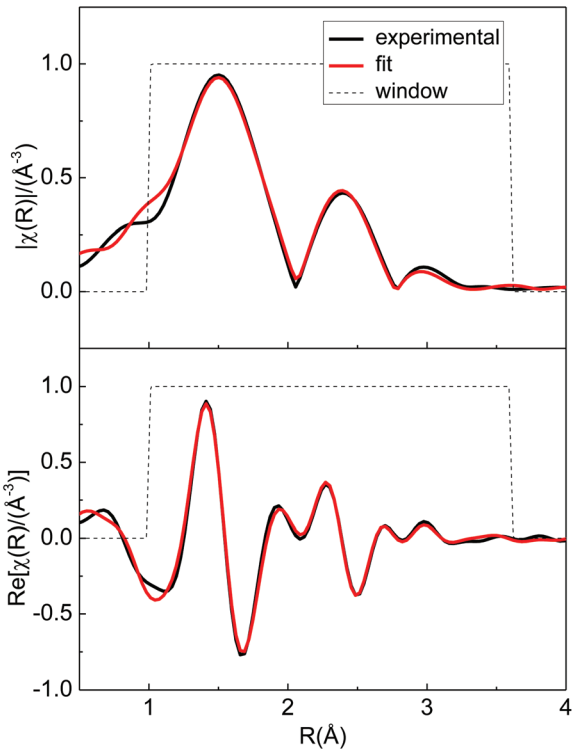

Fig. 9 Fourier transform of EXAFS oscillations at the molybdenum K-edge for amorphous $La_2Mo_2O_{6.72}$: modulus (upper) and real part (lower). Red lines show the fit of EXAFS data with 7 coordination shells around Mo in $La_2Mo_2O_7$.

The summary of the results of the EXAFS fit of the amorphous compound with $La_2Mo_2O_7$ paths is shown in Table 5.

It is worth noting that the displacements with respect to the original positions of the paths in the $La_2Mo_2O_7$ structure are very short, with the exception of the third O2 shell. Note also the large values of mean square displacements of the two La atoms which might indicate that the EXAFS signal in the amorphous compound does not extend up to enough length in *R* as for detecting shells above ~3.2 Å.

Fig. 10 shows a scheme of the coordination shells around Mo for (a) $La_2Mo_2O_7$ and for (b) amorphous $La_2Mo_2O_{6.72}$ obtained from EXAFS analysis within a $La_2Mo_2O_7$ type model of the local order. Visually, the only important displacements are the shift of the third oxygen shell (O2) away from the central Mo and that the last two La shells are slightly closer to Mo than the initially fifth O4 shell.

These results indicate that models 1 and 2, using $La_2Mo_2O_9$ and $La_7Mo_7O_{30}$ paths respectively, yielding equivalent arrangements with a large concentration of O vacancies, are not the only suitable ones to fit the EXAFS spectrum of the amorphous compound. The local arrangement around Mo might be as well very close to that of the crystallized $La_2Mo_2O_7$ compound, which has closer stoichiometry and therefore a similar valence state for Mo. A main difference between model 3 and models

Table 4 Coordination numbers and average distances of the arrangement model based on $La_7Mo_7O_{30}$ paths around Mo, summarized as three main shells

# Main shell	Atom	*N*coor	Average *R*
1st	O	3.36	2.05
Intermediate	O	1.34	2.53
2nd	La	2.86	2.59

Table 5 Single scattering paths calculated for $La_2Mo_2O_7$ (*N* and R_0) and results from fitting the EXAFS spectrum of amorphous $La_2Mo_2O_{6.72}$ (*R*, ΔE_0 and σ^2) with 7 coordination shells of $La_2Mo_2O_7$ around Mo[a]

Atom	*N*	R_0/Å	*R*/Å	σ^2/Å^2
O4	2	1.951	2.172	*0.00341*
O1, O2, O3	3	2.019	2.021	*0.00341*
O2	1	2.082	2.453	*0.00465*
Mo1	1	2.478	2.739	*0.00628*
O4	2	3.263	3.293	*0.00508*
La1	2	3.405	3.285	*0.02384*
La1	2	3.436	3.257	*0.02384*

[a] $S_0^2 = 0.928$; ΔE_0(eV) = 2.709; *R*-factor = 0.0097.

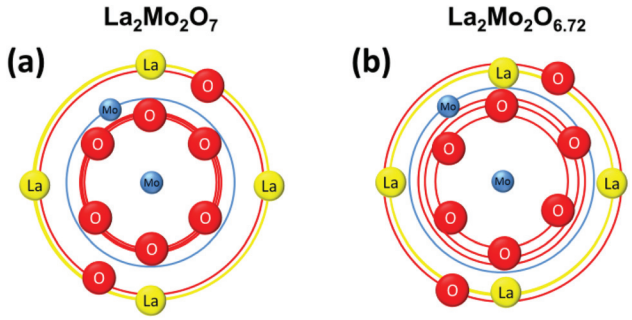

Fig. 10 Schemes of coordination shells around Mo in: (a) crystalline $La_2Mo_2O_7$; (b) amorphous $La_2Mo_2O_{6.72}$ obtained from EXAFS analysis within a $La_2Mo_2O_7$ type model of the local order.

1/2 is the presence, in model 3, of a short Mo–Mo distance (2.74 Å, to be compared to 2.487 Å in $La_2Mo_2O_7$ as reported by Moini *et al.*[27]).

The previous studies show that EXAFS analysis does not seem to be able to discriminate between the local orders of the known crystallized lanthanum molybdates as the best reference for the local order in $La_2Mo_2O_{6.72}$. In order to gain complementary information about it, we carried out EPR measurements on the amorphous compounds.

3.3 EPR analysis of the amorphous form

Paramagnetic molybdenum ions with oxidation states +5 and +3 have the electronic configurations of $[Kr]4d^1$ and $[Kr]4d^3$, respectively. The associated effective electronic spins are S = 1/2 for Mo^{5+} and S = 3/2 for Mo^{3+}. In contrast, due to their diamagnetic valence, Mo^{4+} and Mo^{6+} states cannot be detected by EPR.

For a better resolution, the EPR spectrum of amorphous $La_2Mo_2O_{6.7}$ shown in Fig. 11 has been recorded at 150 K. It potentially shows the presence of two paramagnetic species. The middle part centered around 3500 Gauss fits qualitatively with an S = 1/2 spin possibly attributable to Mo^{5+} ions with an

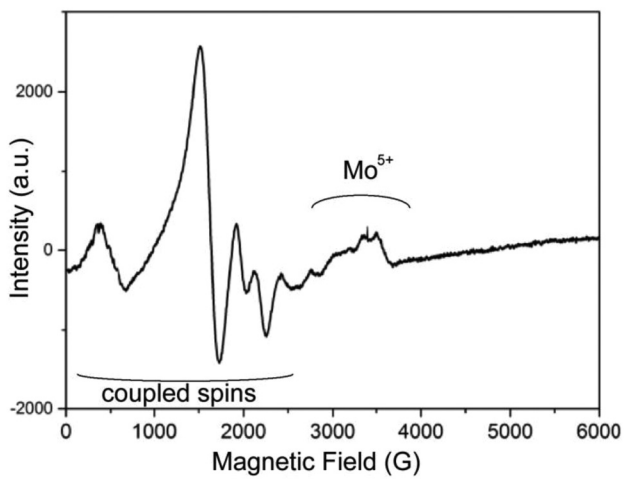

Fig. 11 EPR signal of amorphous $La_2Mo_2O_{6.7}$.

anisotropic g tensor with components g_x = 1.83(2), g_y = 1.89(2), g_z = 2.03(3) and anisotropic EPR linewidths h_x = 100(±10) G, h_y = 70(±10) G, h_z = 50(±10) G. The large uncertainties on the g-tensor components and linewidths are explained in part by the unresolved hyperfine structure (nuclear spin I = 5/2 for ^{95,97}Mo with natural abundance 15.8% and 9.6% respectively). These results can be understood by distorted oxygen environments of Mo^{5+} such as octahedral MoO_6 (g_x = 1.892, $g_y = g_z$ = 1.944) or square-pyramidal MoO_5 (g_x = 1.866, $g_y = g_z$ = 1.957).[36] The absence of resolved hyperfine structures is indicative of a disorder in the molybdenum environments as expressed by the large line widths. The important EPR spectrum part located in the low field side below 3000 G is characteristic of a crystal field interaction involving high spin species such as Mo^{3+} ions or Mo–Mo pairs. However, for the considered sample composition, despite several fitting attempts, no satisfying theoretical simulation of the EPR spectrum was obtained by using S = 1 or S = 3/2 effective spins (as for Mo^{5+}–Mo^{5+} pairs or Mo^{3+} respectively). Considering the good resolution of this low field EPR spectrum, the existence of ion pairs as La–Mo or Mo–Mo, or coupled through vacancies such as Mo–□–Mo with important coupling parameters ($J \approx 1$ cm^{-1}) could be at the origin of the EPR signal.[37] Given that La^{2+} (S = 1/2) is very rare in oxides, and would have an EPR signal with parameters slightly different from Mo^{5+} (which would make it visible in the central part of the spectrum), the existence of isolated La^{2+} can be excluded. The Mo^{3+}–Mo^{3+} pairs (S = 0, 1, 2, 3) are unlikely to be observed above 5–10 K. Therefore the most probable origin of the low field broad bands must be attributed to Mo^{3+}–Mo^{5+} or Mo^{5+}–Mo^{5+} ion pairs. It implies the existence of Mo–Mo short distances. This is in agreement with model 3 described above, derived from the $La_2Mo_2O_7$ arrangement.

3.4 Step by step building of the amorphous model from EXAFS

The results obtained in the previous section seem to point towards model 3 as the most probable arrangement around Mo in the amorphous phase. Nevertheless, the evidence of oxide ion conductivity in this material suggests some preservation of the $La_2Mo_2O_9$ structure, at least regarding part of the oxygen sublattice.

Looking for a simpler model, we have performed a different kind of EXAFS analysis, consisting of fitting the first shell (quick first shell tool in ARTEMIS), and then generating and testing theoretical single scattering shells at suspected distances (SSpaths in ARTEMIS).[38] This way, we have generated and compared multiple configurations.

3.4.1 First shell fit. Assuming reasonably that in the amorphous compound, the first shell around Mo (corresponding roughly to the first peak in the magnitude graph in R-space) consists of oxide ions; a quick first shell has been performed. The coordination number and the average position of O atoms have been estimated this way. The fit is shown in Fig. 12.

The summary of results is listed in Table 6. As observed, the value of the O coordination number, N, is 3.565 at a position of 2.055 Å. This value is in agreement with the first shells

 This journal is © The Royal Society of Chemistry 2017

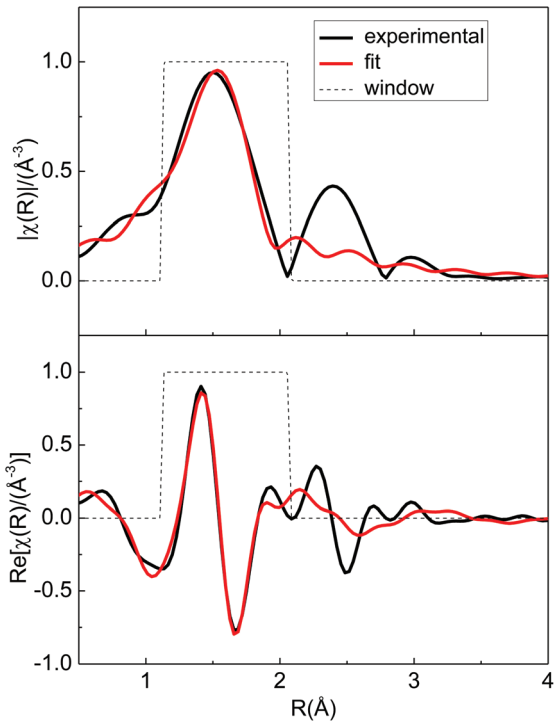

Fig. 12 Fourier transform of EXAFS oscillations at the molybdenum K-edge for amorphous $La_2Mo_2O_{6.72}$: modulus (upper) and real part (lower). Red lines show the first O shell fit.

Table 6 Results from the first shell fit around Mo in amorphous $La_2Mo_2O_{6.72}$ assuming O atoms[a]

Atom	*N*	*R*/Å	σ^2/Å^2
O	*3.57*	*2.06*	*0.0054*

[a] $S_0{}^2 = 0.928$; ΔE_0(eV) = −3.932; *R*-factor = 0.0236.

of both models 1 and 2, but not with model 3, in which the coordination number would yield 4.8 (note that in model 3, there is a O2 shell that moves away from Mo up to ∼2.4 Å).

3.4.2 Single scattering path like construction. After fitting the first coordination shell, we have generated subsequent theoretical shells trying O, Mo or La as scatters. The only shell with non-integer multiplicity was kept to be the first one of O.

The models tested have at most 3 shells: the first O shell at ∼2.0 Å, a second shell of an integer number of La or Mo at ∼2.7 Å and in a few cases an intermediate O shell at ∼2.5 Å. Each shell was generated *via* SSpaths in ARTEMIS using the potential of the FEFF calculation of crystalline β-$La_2Mo_2O_9$. A description of the models used, and the results obtained from the EXAFS fit of the $La_2Mo_2O_{6.72}$ spectrum with each model, are given in Table 7. The modulus of the Fourier Transform of the EXAFS signal of $La_2Mo_2O_{6.72}$ and each fit using SSpaths are shown in Fig. 13.

Models F and G, with 1 and 2 La atoms as second shells, respectively, present large *R*-factors compared to the other fits. Models A, B, C, D and E have Mo in the second shells. Among these fits the two with the best quality are B and E. Both models have a first O shell with ∼3.8 atoms and 2 Mo atoms as a second shell at ∼2.7 Å but model E has an intermediate O shell with 1 atom at ∼2.5 Å. Nevertheless, the mean square displacement σ^2 of this intermediate shell is suspiciously large as compared to those of the other O and the next Mo. The large σ^2 damps significantly the signal of this path so its contribution to the total fit is very weak. It is possible then that this shell is not really present, as in model B, or it is has a very low partial occupancy (O vacancies). Either case would result in an open or (semi-open) space which might be a migration path for O^{2-} ions.

A scheme of model B is shown in Fig. 14 (with 4 O in the first shell); model E would have 1 (or less) O atoms in between the O first shell and Mo shell.

The first O shell in model B (and E) is very similar to that obtained in model 1 (and 2) in the previous section. On the other hand, the presence of a second shell of Mo is in agreement with model 3 (although the multiplicity is not the same) and the results from EPR analysis. One might then understand model B (or E) as a combination of the first shell of model 1 (or 2) and the second shell of model 3. Regarding the intermediate shell, one has to keep in mind that the main difference between models 1 and 2 came from the coordination

Table 7 Models used from SSpaths for EXAFS fitting of amorphous $La_2Mo_2O_{6.72}$ compared to models issued from crystallized phases

		1st shell O			Int O shell			2nd shell					
Model	Description	*N*	*R*/Å	σ^2/Å^2	*N*	*R*/Å	σ^2/Å^2	Atom	*N*	*R*/Å	σ^2/Å^2	*R*-Factor	*N* variables
1	$La_2Mo_2O_9$	3.367	∼2.03	0.0019	2.07	2.54	0.003	La	3	2.58	0.0146	0.0081	11
2	$La_7Mo_7O_{30}$	3.360	∼2.05	0.0028	1.34	2.53	0.001	La	2.57	2.59	0.0130	0.0129	13
3	$La_2Mo_2O_7$	4.800	∼2.08	0.0034	0.96	2.45	0.005	Mo	1	2.74	0.0063	0.0100	13
A	Ox-Mo	3.810	2.04	0.0056				Mo	1	2.73	0.0042	0.0140	6
B	Ox-2Mo	3.836	2.04	0.0059				Mo	2	2.73	0.0084	0.0063	6
C	Ox-3Mo	3.842	2.04	0.0061				Mo	3	2.73	0.0114	0.0081	6
D	Ox-O-Mo	3.878	2.04	0.0058	1	2.58	0.030	Mo	1	2.72	0.0042	0.0133	8
E	Ox-O-2Mo	4.072	2.04	0.0066	1	2.52	0.016	Mo	2	2.72	0.0086	0.0041	8
F	Ox-La	3.348	2.05	0.0038				La	1	2.60	0.0048	0.0278	6
G	Ox-2La	3.238	2.05	0.0038				La	2	2.61	0.0099	0.0433	6

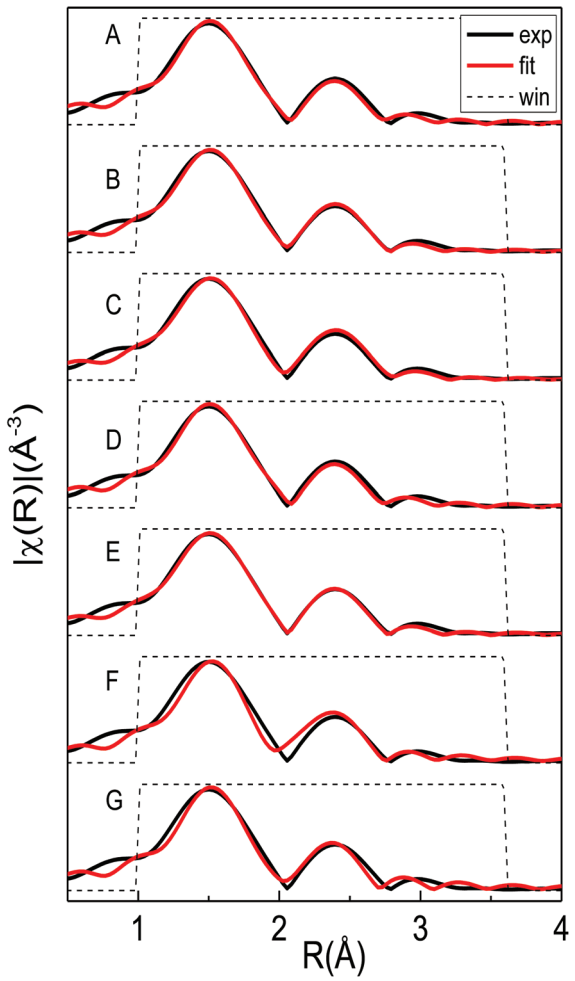

Fig. 13 Modulus of Fourier transform of EXAFS oscillations at the molybdenum K-edge for amorphous $La_2Mo_2O_{6.72}$ with the fits based on seven different arrangements generated by SSpaths.

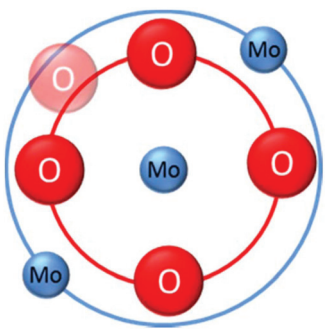

Fig. 14 Scheme of coordination shells around Mo in amorphous $La_2Mo_2O_{6.72}$ with models B or E of SSpaths EXAFS analysis.

number of the intermediate O shells at around 2.5 Å, so this uncertainty is common in all models (even in model 3) which reinforces the hypothesis of a not fully occupied shell.

The simplicity of the model schemed in Fig. 14 with less variable parameters and better reliability than any model based on crystallized forms, the agreement with EPR results and the underlying presumption of a large concentration of O vacancies between shells lead us to propose this model as the most accurate for describing the short length order around Mo in the amorphous compound studied.

4. Summary and conclusion

After being severely reduced in flowing Ar–H_2 at 608° C for 2 days or 700 °C for 9 h, $La_2Mo_2O_9$ powder samples become amorphous with a composition close to $La_2Mo_2O_{6.7}$. Such an amorphous phase was previously shown to be interesting as an anode material in SOFC devices due to both its mixed ionic-electronic conductivity and tolerance to sulphur. In this paper, we used successively XRD, EPR and EXAFS analyses to gain better insight into the local structural arrangement of this amorphous phase.

The crystallographic data of crystalline phases with an intermediate oxygen content between $La_2Mo_2O_9$ and $La_2Mo_2O_{6.7}$, namely $La_7Mo_7O_{30}$ and $La_2Mo_2O_7$ were first used. Amorphous types of XRD patterns were obtained for the 3 crystalline phases by simulating their XRD diagrams after having reduced the coherence length to a few angströms. In all three cases, the resulting pattern is very close to the one recorded on amorphous $La_2Mo_2O_{6.7}$, which prevents from reaching any firm conclusion about a possible similarity between the local environment of the amorphous phase and that of one of the crystalline phases.

The main part of this study was devoted to EXAFS analyses of the amorphous phase at the Mo K-edge. The local arrangements around Mo of the three mentioned crystal structures were used as models to fit (or compare with) the $La_2Mo_2O_{6.72}$ spectrum. Fitting using paths calculated from crystalline $La_2Mo_2O_9$ and $La_7Mo_7O_{30}$ structures yields very similar local arrangements around Mo for the amorphous phase. This is in spite of the obvious differences between the crystalline structures and the number of paths included for each model in the analysis window. Using $La_2Mo_2O_7$ as the initial model also leads to a good fit of the EXAFS spectrum of the amorphous compound with a short Mo–Mo distance. This last model is in agreement with EPR analysis. Indeed, the EPR spectrum of $La_2Mo_2O_{6.7}$ shows two main signals, one centered around 3500 Gauss characteristic of Mo^{5+} ions, and a second intense and well resolved contribution at a lower magnetic field. These features are attributed to a higher spin state which can only originate from spin pairs. It therefore seems that the most probable configuration consistent with the EPR spectrum corresponds to either Mo^{3+}–Mo^{5+} or Mo^{5+}–Mo^{5+} pairs, hence to short Mo–Mo distances.

On the other hand, a simpler model for the EXAFS fit, built from theoretical single scattering paths, suggests that Mo is surrounded by ~3.8 O atoms, then another O shell which is barely occupied, and a Mo shell with most likely 2 atoms. The intermediate O shell would have a large concentration of O vacancies which could give a path for oxide ion migration. The presence of a Mo shell at the short distance of 2.7 Å would also explain the signal observed in the EPR spectrum. One has

 This journal is © The Royal Society of Chemistry 2017

however to be careful in our interpretations. EPR does not provide an overall balanced view of the ionic repartition in the observed phase, since it focuses on those elements that are detected by the magnetic probe, which can be in a very small amount in the sample (down to a few ppms). The presence of molybdenum pairs is nevertheless consistent with the efficiency of the amorphous phase as the anode material in a SOFC, since distant Mo centers would involve moderate electronic conductivity (as a matter of fact $La_2Mo_2O_7$ is a metal at room temperature[27]). The best model issued from EXAFS analysis suggests that in amorphous $La_2Mo_2O_{6.7}$, short Mo–Mo distances are not limited to pairs, but extend to triplets, at least. The gradual concentration of Mo atoms when $La_2Mo_2O_9$ is reduced is consistent with the appearance of metallic molybdenum particles upon further reduction of the amorphous phase.[39]

Acknowledgements

This work has been supported by the Brazilian Synchrotron Light Laboratory (LNLS)/Brazilian Biosciences National Laboratory (LNBio) under proposal XAFS1 12685. Thanks to Dr Eduardo Granado for measuring the XAS spectra at the XDS line in LNLS. J. Vega-Castillo thanks Ifeffit mailing list members especially Dr Bruce Ravel and Dr Matt Newville.

References

1 P. Lacorre, F. Goutenoire, O. Bohnke, R. Retoux and Y. Laligant, *Nature*, 2000, **404**, 856–858.
2 C. Tealdi, G. Chiodelli, L. Malavasi and G. Flor, *J. Mater. Chem.*, 2004, **14**, 3553–3557.
3 D. Marrero-López, D. Pérez-Coll, J. C. Ruiz-Morales, J. Canales-Vázquez, M. Martín-Sedeño and P. Núñez, *Electrochim. Acta*, 2007, **52**, 5219–5231.
4 X. Wang, Z. Cheng and Q. Fang, *Solid State Ionics*, 2005, **176**, 761–765.
5 A. Subramania, T. Saradha and S. Muzhumathi, *Mater. Chem. Phys.*, 2007, **167**, 319–324.
6 S. Georges, F. Goutenoire, F. Altorfer, D. Sheptyakov, F. Fauth, E. Suard and P. Lacorre, *Solid State Ionics*, 2003, **161**, 231–241.
7 D. Marrero-López, J. Canales-Vázquez, W. Zhou, J. T. S. Irvine and P. Núñez, *J. Solid State Chem.*, 2006, **179**, 278–288.
8 D. Marrero-López, J. C. Ruiz-Morales, D. Pérez-Coll, P. Núñez, J. C. C. Abrantes and J. R. Frade, *J. Solid State Electrochem.*, 2004, **8**, 638–643.
9 V. I. Voronkova, E. P. Kharitonova and A. E. Krasil'nikova, *Crystallogr. Rep.*, 2010, **55**, 276–282.
10 S. Basu, P. S. Devi and H. S. Maiti, *J. Electrochem. Soc.*, 2005, **152**, 2143–2147.
11 Z. S. Khadasheva, N. U. Venskovskii, M. G. Safronenko, A. V. Mosunov, E. D. Politova and S. Y. Stefanovich, *Inorg. Mater.*, 2002, **38**, 1168–1171.
12 G. Corbel, Y. Laligant, F. Goutenoire, E. Suard and P. Lacorre, *Chem. Mater.*, 2005, **17**, 4678–4684.
13 A. Arulraj, F. Goutenoire, M. Tabellout, O. Bohnke and P. Lacorre, *Chem. Mater.*, 2002, **14**, 2492–2498.
14 J. A. Collado, M. A. G. Aranda, A. Cabeza, P. Olivera-Pastor and S. Bruque, *J. Solid State Chem.*, 2002, **167**, 80–85.
15 A. Selmi, C. Galven, G. Corbel and P. Lacorre, *Dalton Trans.*, 2010, **39**, 93–102.
16 J. Jacquens, D. Farrusseng, S. Georges, J.-P. Viricelle, C. Gaudillère, G. Corbel and P. Lacorre, *Fuel Cells*, 2010, **10**, 433–439.
17 G. Corbel, E. Chevereau, S. Kodjikian and P. Lacorre, *Inorg. Chem.*, 2007, **46**, 6395–6404.
18 G. Corbel, P. Durand and P. Lacorre, *J. Solid State Chem.*, 2009, **182**, 1009–1016.
19 X. C. Lu and J. H. Zhu, *J. Electrochem. Soc.*, 2008, **155**, B1053–B1057.
20 G. Buvat, E. Quarez and O. Joubert, *J. Power Sources*, 2016, **302**, 107–113.
21 W. Liu, W. Pan, J. Luo, A. Godfrey, G. Ou, H. Wu and W. Zhang, *Nat. Commun.*, 2015, **6**, 8354–8362.
22 A. Caneiro, *Rev. Sci. Instrum.*, 1982, **53**, 1072.
23 J. E. Vega-Castillo, U. K. Ravella, G. Corbel, P. Lacorre and A. Caneiro, *Dalton Trans.*, 2012, **41**, 7266–7271.
24 J. E. Vega-Castillo, U. K. Ravella, G. Corbel, P. Lacorre and A. Caneiro, *Dalton Trans.*, 2014, **43**, 2661–2669.
25 B. Ravel and M. Newville, *J. Synchrotron Radiat.*, 2005, **12**, 537–541.
26 F. Goutenoire, R. Retoux, E. Suard and P. Lacorre, *J. Solid State Chem.*, 1999, **142**, 228–235.
27 A. Moini, M. A. Subramanian, A. Clearfield, F. J. DiSalvo and W. H. McCarroll, *J. Solid State Chem.*, 1987, **66**, 136–143.
28 ICDD, *PDF-4+ 2009 (Database)*, 12 Campus Boulevard, Newtown Square, Pennsylvania 19073-3273, U.S.A., 2009.
29 J. Vega-Castillo, L. Mogni, G. Corbel, P. Lacorre and A. Caneiro, *Int. J. Hydrogen Energy*, 2010, **35**, 5890–5894.
30 P. Lacorre and R. Retoux, *J. Phys. Chem. Solids*, 1997, **132**, 443–446.
31 S. Zabinsky, J. Rehr, A. Ankudinov, R. Albers and M. Eller, *Phys. Rev. B: Condens. Matter*, 1995, **52**, 2995–3009.
32 I. R. Evans, J. a. K. Howard and J. S. O. Evans, *Chem. Mater.*, 2005, **17**, 4074–4077.
33 L. Malavasi, H. Kim, S. J. L. Billinge, T. Proffen, C. Tealdi and G. Flor, *J. Am. Chem. Soc.*, 2007, **129**, 6903–6907.
34 F. Goutenoire, O. Isnard, R. Retoux and P. Lacorre, *Chem. Mater.*, 2000, **12**, 2575–2580.
35 R. D. Shannon, *Acta Crystallogr., Sect. A: Cryst. Phys., Diffr., Theor. Gen. Cryst.*, 1976, **32**, 751–767.
36 M. Che, C. Louis and Z. Sojka, *J. Chem. Soc., Faraday Trans. 1*, 1989, **85**, 3939–3952.
37 K. Marney, A. H. Francis, G. L. McPherson and P. J. McCarthy, *J. Phys.: Condens. Matter*, 1992, **4**, 535–544.
38 J. J. J. Rehr and R. C. Albers, *Rev. Mod. Phys.*, 2000, **72**, 621–654.
39 G. Buvat, H. Sellemi, U. K. Ravella, M. Barré, S. Coste, G. Corbel and P. Lacorre, *Inorg. Chem.*, 2016, **55**, 2522–2533.